Novel P-n Li$_2$SnO$_3$/g-C$_3$N$_4$ Heterojunction With Enhanced Visible Light Photocatalytic Efficiency Toward Rhodamine B Degradation

Yuanyuan Li*, Meijun Wu[1], Yaoqiong Wang[2], Qimei Yang[1], Xiaoyan Li[3], Bin Zhang[4]* and Dingfeng Yang[2]*

[1] Department of Biological and Chemical Engineering, Cooperative Innovation Center of Lipid Resources and Children's Daily Chemicals, Chongqing University of Education, Chongqing, China, [2] College of Chemistry and Chemical Engineering, Chongqing University of Technology, Chongqing, China, [3] National ad Local Joint Laboratory of Traffic Civil Engineering Materials, Department of Materials and Engineering, Chongqing Jiaotong University, Chongqing, China, [4] Analytical and Testing Center of Chongqing University, Chongqing, China

The design of highly efficient and stable photocatalysts to utilize solar energy is a significant challenge in photocatalysis. In this work, a series of novel p-n heterojunction photocatalysts, Li$_2$SnO$_3$/g-C$_3$N$_4$, was successfully prepared via a facile calcining method, and exhibited superior photocatalytic activity toward the photodegradation of Rhodamine B solution under visible light irradiation as compared with pure Li$_2$SnO$_3$ and g-C$_3$N$_4$. The maximum kinetic rate constant of photocatalytic degradation of Rhodamine B within 60 min was 0.0302 min^{-1}, and the composites still retained excellent performance after four successive recycles. Chemical reactive species trapping experiments and electron paramagnetic resonance demonstrated that hydroxyl radicals ($\cdot$OH) and superoxide ions ($\cdot$O$_2^-$) were the dominant active species in the photocatalytic oxidation of Rhodamine B solution, while holes (h$^+$) only played a minor role. We demonstrated that the enhancement of the photocatalytic activity could be assigned to the formation of a p-n junction photocatalytic system, which benefitted the efficient separation of photogenerated carriers. This study provides a visible light-responsive heterojunction photocatalyst with potential applications in environmental remediation.

Keywords: Li$_2$SnO$_3$, g-C$_3$N$_4$, p-n heterojunction, photocatalysis, Rhodamine B, Photoelectrochemistry

INTRODUCTION

The presence of harmful and toxic substances in aqueous solution poses severe risks to human health and ecosystems. The purification of waste water is an urgent priority and a major research theme in environmental science (Shannon et al., 2008; Damasiewicz et al., 2012). As a promising technique for oxidation of pollutants, semiconductor-based photocatalysis, which uses solar energy to drive chemical reactions, has an important role in environmental remediation (Chen et al., 2010). Among semiconductor photocatalysts, layered metal oxides have attracted much attention owing to their low cost, photostability, and oxidation capability (Osada and Sasaki, 2009; Lei et al., 2014; Haque et al., 2018).

Recently, the semiconductor Li$_2$SnO$_3$ has been applied as a UV light-responsive photocatalyst with excellent photocatalytic performance and chemical stability (Li Y. Y. et al., 2019). As a

state-of-the-art layered photocatalyst, the compound features a conventional [Li$_{1/3}$Sn$_{2/3}$O$_2$]$^-$ anion layered structure in the *a-b* planes, while the rest of the Li$^+$ cations embed in the interlayer spaces to balance the charge (Howard and Holzwarth, 2016). The resulting charge density distribution in space generates an electrostatic field perpendicular to the laminar direction, promoting the separation of photo-induced carriers to drive photocatalysis. In addition, the valence band edge of Li$_2$SnO$_3$ is positive enough to oxidize organic pollutants. However, similar to many other oxide semiconductors, Li$_2$SnO$_3$ can only absorb UV light, while its harvesting of solar energy is poor owing to its wide intrinsic optical band gap (∼3.7 eV), limiting its photocatalytic activity. Constructing visible light-responsive Li$_2$SnO$_3$-based heterojunction photocatalysts to make full use of sunlight is thus an important goal. This kind of system, where a heterojunction is formed between a visible light- and a UV light-responsive photocatalyst, has received some attention in recent years (Pan et al., 2012; Li et al., 2017; Wu et al., 2017; Liu et al., 2018; Qiao et al., 2018; Wang et al., 2018a; Hafeez et al., 2019). For instance, ZnFe$_2$O$_4$/TiO$_2$ heterojunctions exhibited outstanding photocatalytic degradation of bisphenol A under visible light irradiation (Nguyen et al., 2019). A CdS/SrTiO$_3$ nanodots-on-nanocubes heterojunction presented excellent visible light photocatalytic performance for oxidation of H$_2$ (Yin et al., 2019). Notably, Dong et al. successfully synthesized an insulator-based core-shell SrCO$_3$/BiOI heterojunction structure, and this nanocomposite displayed an unprecedentedly high photocatalytic NO removal performance (Wang et al., 2018b). Therefore, the heterojunction strategy clearly provides opportunities to utilize wide-band-gap semiconductors with excellent intrinsic photophysical properties as visible light-responsive photocatalysts.

Among the best known classes of such catalysts are *p-n* heterojunctions, which have been extensively studied to optimize their photocatalytic activity. Their catalytic mechanism is based on an internal electric field established at the interface of the *p-n* junction, which promotes the efficient separation of photogenerated carriers (Wen X. J. et al., 2017; Dong et al., 2018; Dursun et al., 2018; Wang et al., 2018; Zeng et al., 2019). The Mott-Schottky plots measured by electrochemistry demonstrate that Li$_2$SnO$_3$ is a *p*-type semiconductor. Therefore, to improve its photocatalytic performance, it is necessary to couple Li$_2$SnO$_3$ with *n*-type and visible light-responsive semiconductors to build *p-n* heterojunction systems, which would be able to simultaneously realize high utilization rates of solar energy and efficient separation of photogenerated carriers. Among numerous *n*-type photocatalytic semiconductors, g-C$_3$N$_4$ is a promising candidate for its tunable photo-response, and effective charge carrier transportation properties. As a photocatalyst, g-C$_3$N$_4$ has been widely investigated owing to its excellent properties including layered graphite-like structure, visible light-responsive band gap (∼2.7 eV), facile preparation, low toxicity, and high photostability (Wang et al., 2009, 2019; Ong et al., 2016; Wen J. Q. et al., 2017; Lu et al., 2018; Zhang et al., 2018; Li X. B. et al., 2019). Furthermore, as an *n*-type semiconductor, g-C$_3$N$_4$ has been selected to be coupled with *p*-type semiconductors to enhance photocatalytic activity, such as in CuBi$_2$O$_4$/g-C$_3$N$_4$

(Guo et al., 2017), Bi$_4$Ti$_3$O$_{12}$/g-C$_3$N$_4$ (Guo et al., 2016), and LaFeO$_3$/g-C$_3$N$_4$ (Liang et al., 2017).

EXPERIMENTAL SECTION

Synthesis of G-C$_3$N$_4$, Li$_2$SnO$_3$, and Li$_2$SnO$_3$/g-C$_3$N$_4$ Heterojunction

g-C$_3$N$_4$ was prepared by annealing melamine in a muffle furnace. Briefly, 5 g melamine was heated in an closed crucible at a rate of 4.5°C/min to 560°C and maintained for 2 h. Then, the furnace was turned off and cooled to room temperature naturally. Pure Li$_2$SnO$_3$ was synthesized from a mixture of Li$_2$CO$_3$ and SnO$_2$ with a molar ratio of 3.3/3.0. The mixed reactants were ground together within a mortar for 30 min. Then, the mixture was heated at 850°C for 6 h. The heterojunctions Li$_2$SnO$_3$/g-C$_3$N$_4$ (LSO-CN) with different mass ratios were prepared by a traditional solid state method. Samples with initial mass ratios of g-C$_3$N$_4$ to LSO-CN having values of 70, 80, 85, 90, and 95 wt% were prepared, and labeled as LSO-CN-70, LSO-CN-80, LSO-CN-85, LSO-CN-90, and LSO-CN-95, respectively. Taking LSO-CN-85 as an example, 0.03 g of Li$_2$SnO$_3$ powder, 0.17 g of g-C$_3$N$_4$ and 1 mL ethanol were mixed, and ground together for 10 min. The resultant mixture was heated at 500°C for 2 h in a covered crucible.

Characterization

Powder X-ray diffraction (PXRD) was performed on a PANalytical X'pert powder diffractometer equipped with a PIXcel detector and with CuKα radiation (40 kV and 40 mA). The scanning step width of 0.01° and the scanning rate of 0.1° s^{-1} were applied to record the patterns in the 2θ range of 6–90°. A JEOL JSM-6700F field emission scanning electron microscope (SEM) was employed to investigate the surface morphologies. The transmission electron microscopy (TEM) and high-angle annular dark field (HAADF) images and energy-dispersive spectra (EDS) of Li$_2$SnO$_3$ were recorded by a Talos F200S G2 Microscope to characterize the microstructures of the samples. The UV-vis diffuse reflectance spectroscopy (UV-vis DRS) data were collected at room temperature using a powder sample with BaSO$_4$ as a standard on a Shimadzu UV-3150 spectrophotometer over the spectral range 200–800 nm. The Fourier transform infrared (FT-IR) spectra were obtained by using a Nicolet 360 spectrometer with a 2 cm^{-1} resolution in the range of 500–4,000 cm^{-1}. Fluorescence spectra were measured on a Hitachi fluorescence spectrophotometer F-7000 to detect the concentration of, in which the fluorescence emission spectrum (excited at 316 nm) of the solution was measured every 15 min during the photocatalytic reaction. The solid-state photoluminescence (PL) spectra were acquired using a Fluorolog-TCSPC luminescence spectrometer with an excitation wavelength of 325 nm. In the electron paramagnetic resonance(EPR) experiments, 10 mg of LSO-CN-85 sample and 40 μ L of 5,5 Dimethyl-1-pyrroline N-oxide (DMPO) was dispersed into 1 mL of deionized water (DMPO-·OH) or methol (DMPO-·O$_2^-$), and then irradiated with visible light (λ > 420 nm) for 5 and 10 min, respectively. Electrochemical measurement was conducted on a CHI 660E workstation. A

Pt plate, a calomel electrode and sample LSO-CN-85 coated on indium tin oxide (ITO) served as the counter electrode, reference electrode and working electrode, respectively, in a three-electrode cell. Electrochemical impedance spectroscopy (EIS) was carried out using an alternating voltage of 5 mV amplitude over the frequency range of 10^5-0.1 Hz with an open circuit voltage in 0.5 M Na_2SO_4. For the analysis of transient photocurrent responses, a 300-W Xe lamp (cut-off $\lambda > 420$ nm; CEL-HXF300, Beijing Aulight) and Na_2SO_4 were employed as the light source and electrolyte, respectively. The Mott-Schottky curves were measured in Na_2SO_4 solution and the amplitude perturbation was 5 mV with frequencies of 1,000 Hz.

Photocatalytic Activity Measurement

The photocatalytic performance of the LSO-CN composites was evaluated by the degradation of RhB. The light irradiation source was the above-mentioned Xe lamp with a filter ($\lambda \geq$ 420 nm) laid on the top of the reaction vessel. The light source was kept 7 cm away from the top of the reaction vessel and the reactant solution was maintained at room temperature by providing a flow of cooling water during the photocatalytic reaction. Before irradiation, the photocatalyst powder (30 mg) and RhB solution (10 mg L^{-1}, 100 mL) were fully stirred in the dark for 1 h to establish the adsorption–desorption equilibrium. Then, the reaction was exposed to the light, and 5 mL samples of the suspension were extracted at a given time interval and separated by centrifugation. The concentration of RhB solution was determined by UV-vis spectrometry at its maximum absorption peak of 554 nm. Typically, the trapping experiments of active species were carried out as follows: 30 mg LSO-CN-85 and dye solution (10 mg/L, 100 mL) were mixed. Then, 10 mL 2-propanol (IPA), 0.1 mmol disodium ethylenediaminetetraacetic acid (EDTA), and 0.1 mmol ascorbic acid were added in sequence to trap radicals, holes (h^+) and radicals, respectively. Additionally, trapping experiments under fluorescence spectroscopy were carried out as follows: 30 mg

LSO-CN-85 and 8.3 mg terephthalic acid (TA) were dissolved in 100 mL NaOH solution (2 mmol/L), then the solution was stirred for 60 min in the dark and irradiated by the 300-W Xe lamp.

Results and Discussion

The crystallographic structure and phase purity of the as-synthesized samples were confirmed by PXRD. As presented in **Figure 1**, one small peak at 13.1 and one strong peak at 27.4 for pure g-C₃N₄ were assigned to the (100) and (002) crystal plane, respectively, in good accordance with previous reports (Hou et al., 2013). For Li₂SnO₃, the XRD pattern matched well with the monoclinic phase (JCPDS No. 00-031-0761). The two characteristic peaks of g-C₃N₄ gradually decreased in intensity with the increase of the Li₂SnO₃ content in the LSO-CN composites, whereas the peak intensity of Li₂SnO₃ strengthened gradually, reflecting the co-existence of Li₂SnO₃ and g-C₃N₄ in these heterojunctions. Further, the compositions of Li₂SnO₃, g-C₃N₄ and the LSO-CN heterojunction photocatalysts were confirmed by FT-IR. As shown in **Figure 1B**, for pure Li₂SnO₃, characteristic absorption peaks appeared at 519, 1,430, 1,495, and 3,435 cm^{-1}, and the peak located at 519 cm^{-1} was assigned to the stretching vibration of Sn-O-Sn and Sn-O groups (Wang et al., 2012). In the FT-IR spectrum of g-C₃N₄, the peak located at 807 cm^{-1} was assigned to the breathing vibration mode of triazine units. The absorption peaks in the range of 1,000–1,800 cm^{-1} were ascribed to the C=N and aromatic C-N stretching vibration modes, whereas the peaks ranging from 3,000 to 3,500 cm^{-1} originated from the N-H stretching vibrations. The main characteristic peaks of the heterojunctions LSO-CN were similar to those of pure g-C₃N₄ because of the relatively weak vibration intensity of Li₂SnO₃. Notably, however, compared with the g-C₃N₄, the characteristic peaks at 1,241, 1,320, 1,413, and 1,631 cm^{-1} of sample LSO-CN-85 were shifted to higher wavenumbers, which indicated possible interfacial interactions involving electron transfer in these LSO-CN heterostructures (**Figure S1**).

FIGURE 1 | (A) XRD patterns, **(B)** FT-IR spectra of g-C₃N₄, Li₂SnO₃, and LSO-CN heterojunctions.
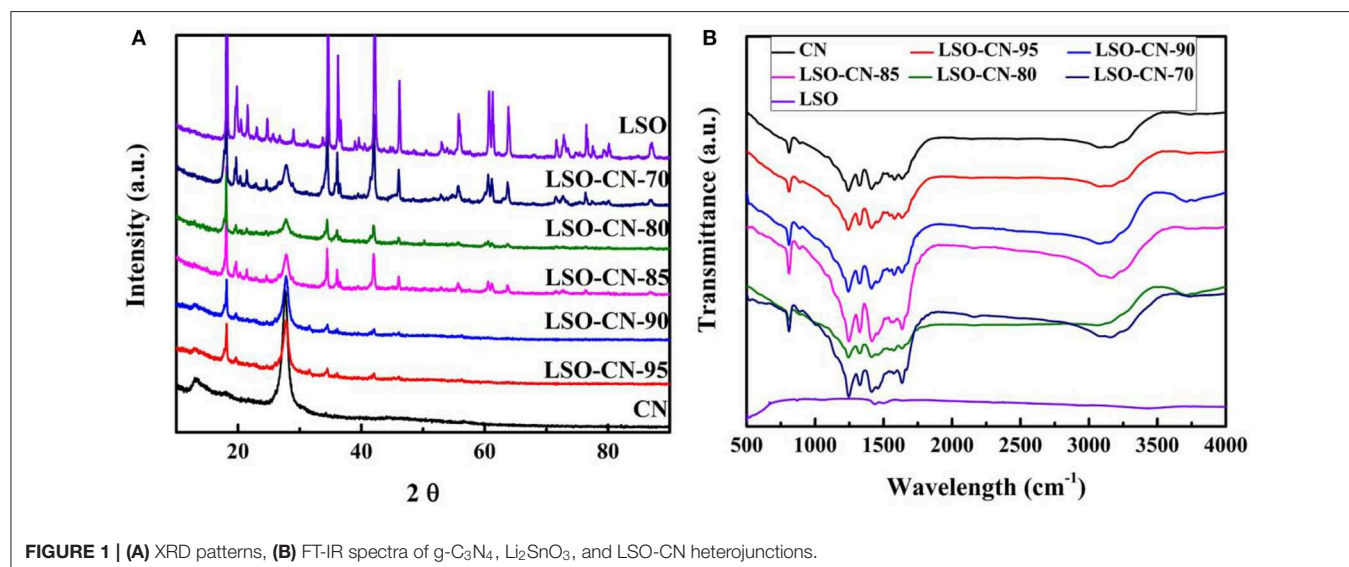
SEM measurements were carried out to examine the morphology of the as-synthesized photocatalysts. Evidently, the as-prepared Li$_2$SnO$_3$ photocatalysts (**Figure 2a**) exhibited irregular bulk morphologies with an average particle length of ~6 μm. **Figure 2b** presents the existence of large aggregates of g-C$_3$N$_4$ with a folded thin-sheet morphology. After combining Li$_2$SnO$_3$ and g-C$_3$N$_4$ into a heterojunction, irregular aggregates of Li$_2$SnO$_3$ were observed to adhere to g-C$_3$N$_4$ (**Figure 2c**), and the SEM-EDS element mapping showed a homogeneous distribution of Sn, O, C and N throughout the heterojunction (**Figure 2d**).

The intimate contact at the heterojunction between Li$_2$SnO$_3$ and g-C$_3$N$_4$ can be further observed in the representative HAADF-TEM image in **Figure 3a**. Meanwhile, the interface formed after the addition of Li$_2$SnO$_3$ into the LSO-CN-85 heterojunction can be clearly seen in the HRTEM image (**Figure 3b**). Notably, no distinct lattice fringes could be observed in g-C$_3$N$_4$ because of its low crystallinity, whereas distinct lattice fringes with a lattice spacing of 0.25 and 0.29 nm were found in Li$_2$SnO$_3$, which were ascribed to the (131) and (−113) planes, respectively. This kind of heterojunction system would be expected to reduce the recombination probability of photo-induced carriers and improve the photocatalytic activity. Additionally, TEM-EDS elemental mapping was performed to further authenticate the hybridization of the *p*-type and *n*-type semiconductors. As presented in **Figure 3c**, the elements Sn, O, C, and N were distributed uniformly across the assemblies, in good accordance with the results of SEM-EDS. In summary, the above analysis by powder XRD, FT-IR, SEM, and TEM manifested that a heterojunction interface was successfully formed in the composite between Li$_2$SnO$_3$ and g-C$_3$N$_4$.

The light absorption ability of the as-prepared samples was determined via UV-vis reflectance spectroscopy to evaluate the optical band gaps. As shown in **Figure 4A**, pure Li$_2$SnO$_3$ presented a typical absorption edge at ~340 nm, and the estimated band gap energy E_g was about 3.64 eV (**Figure 4B**, black trace). For the pure g-C$_3$N$_4$ (**Figure 4A**, red trace), the absorption edge was extended to 451 nm, and the corresponding calculated optical band gap E_g was 2.75 eV (**Figure 4B**, red trace). The obtained E_g values of Li$_2$SnO$_3$ and g-C$_3$N$_4$ were in excellent accordance with previous reports (Wang et al., 2012; Guo et al., 2017). Compared with the pure g-C$_3$N$_4$, when Li$_2$SnO$_3$ was composited with g-C$_3$N$_4$, the LSO-CN-85 heterojunction displayed a blue shift of the absorption band, which would be favorable for efficient separation of the photo-induced carriers, thus leading to a higher photocatalytic performance.

The photocatalytic activities of the as-synthesized samples were evaluated by RhB photodegradation under visible light (λ ≥ 420 nm). The measured photocatalytic activities of the LSO-CN composites are presented in **Figure 5**. As can be seen in **Figure 5A**, without catalysts, the photodegradation of RhB solution under visible light was almost undetectable. The photodegradation rate in the presence of Li$_2$SnO$_3$ alone was only slightly higher, attributed to its wide intrinsic optical band gap. Meanwhile, pure g-C$_3$N$_4$ achieved the modest photodegradation rate of just 36% within 60 min irradiation. However, the photocatalytic activity of g-C$_3$N$_4$/Li$_2$SnO$_3$ was
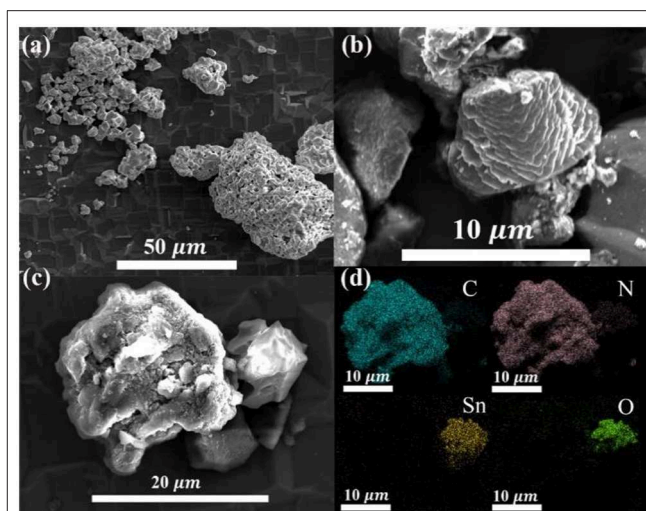

FIGURE 2 | SEM micrographs of **(a)** Li$_2$SnO$_3$, **(b)** g-C$_3$N$_4$, **(c)** LSO-CN-85, and **(d)** element mapping of heterojunction LSO-CN-85.
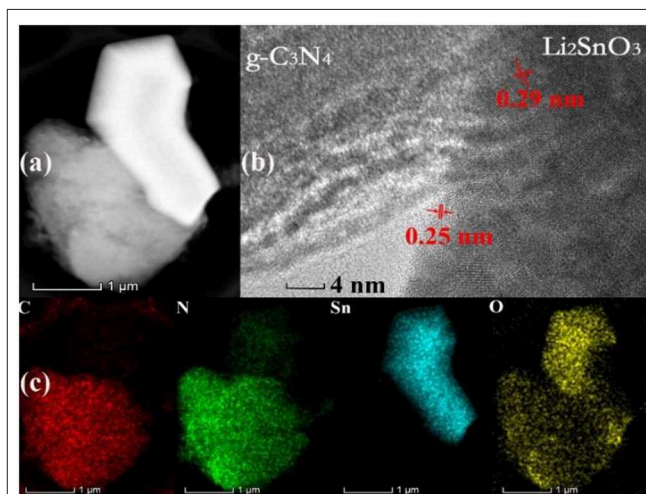

FIGURE 3 | Heterojunction LSO-CN-85: **(a)** HAADF-TEM, **(b)** HRTEM, and **(c)** elemental mapping.

remarkably influenced by the Li$_2$SnO$_3$ content, and all of the LSO-CN composites exhibited superior photocatalytic activities for RhB photodegradation compared with the parent compounds g-C$_3$N$_4$ and Li$_2$SnO$_3$. Among these composites, LSO-CN-85 had the optimal photocatalytic activity, with a photocatalytic degradation efficiency of 86% under visible light within 60 min. **Figure 5B** presents the photocatalytic reaction kinetics of the as-synthesized samples, in which the experimental data can be described by a pseudo-first order model expressed by the following formula (Hailili et al., 2018; Xie et al., 2018):
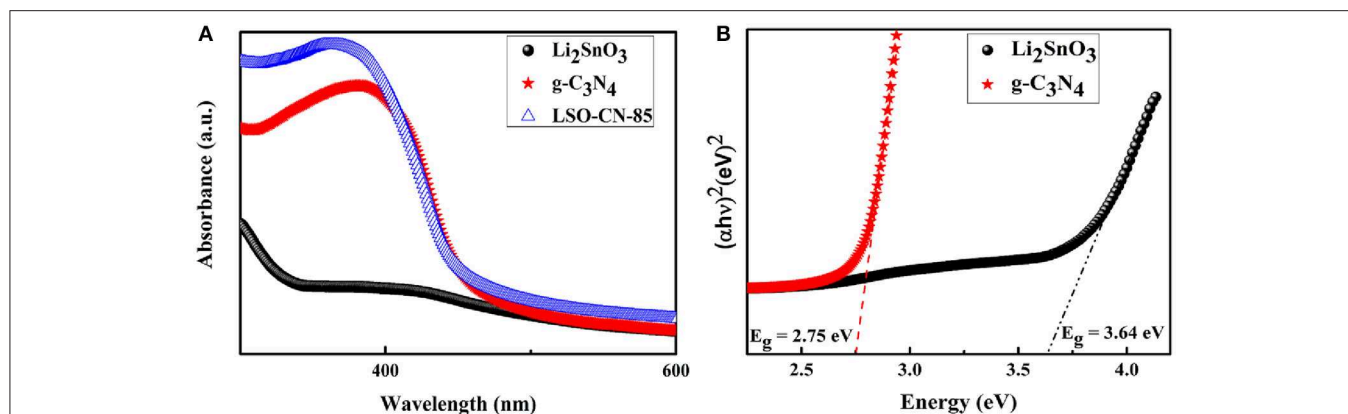
$$-\ln\frac{C}{C_0} = kt$$

FIGURE 4 | (A) UV-vis spectra of Li$_2$SnO$_3$, g-C$_3$N$_4$ and LSO-CN-85 **(B)** Plots of $(\alpha h\nu)^2$ vs. photon energy ($h\nu$) to calculate the band gap energies for Li$_2$SnO$_3$ and g-C$_3$N$_4$.
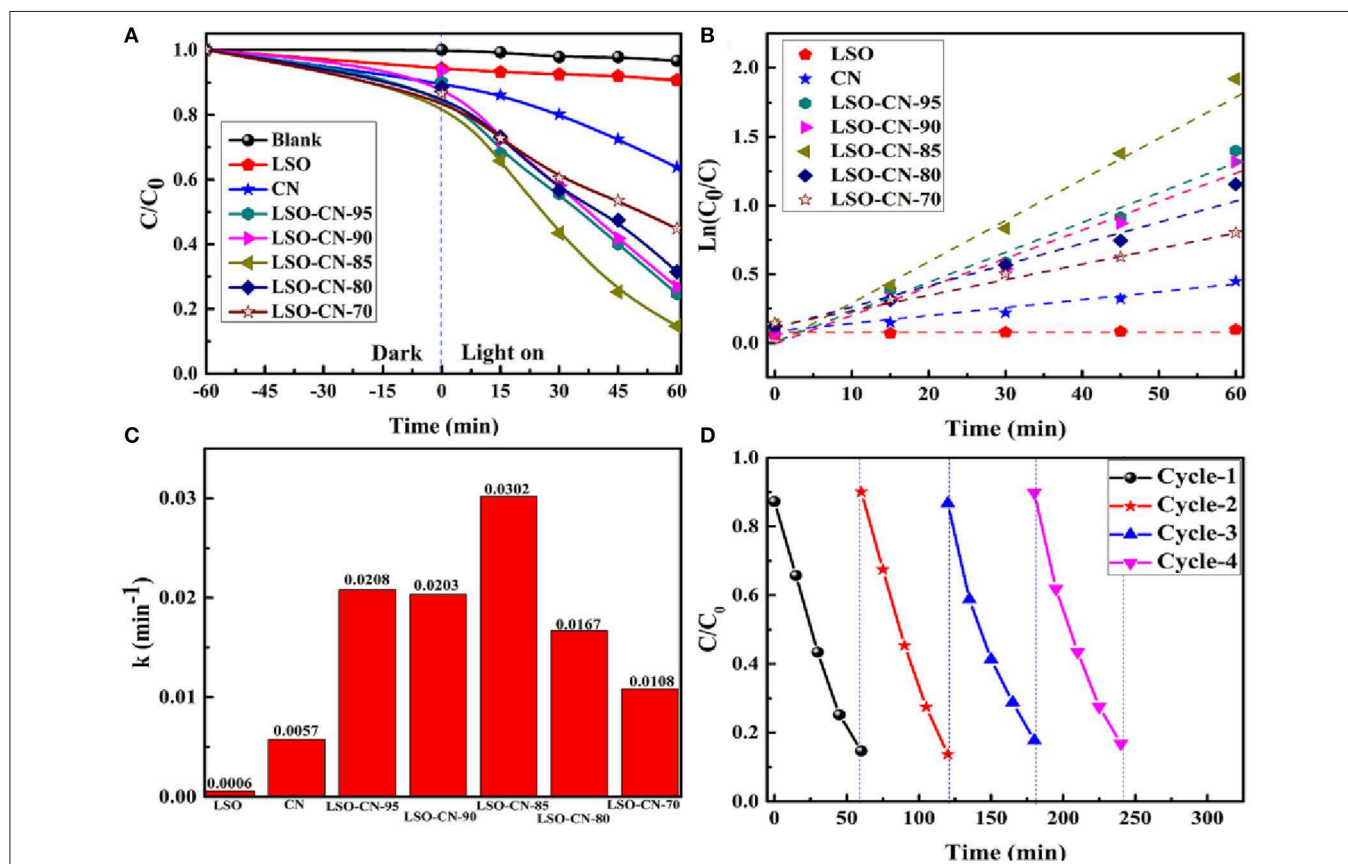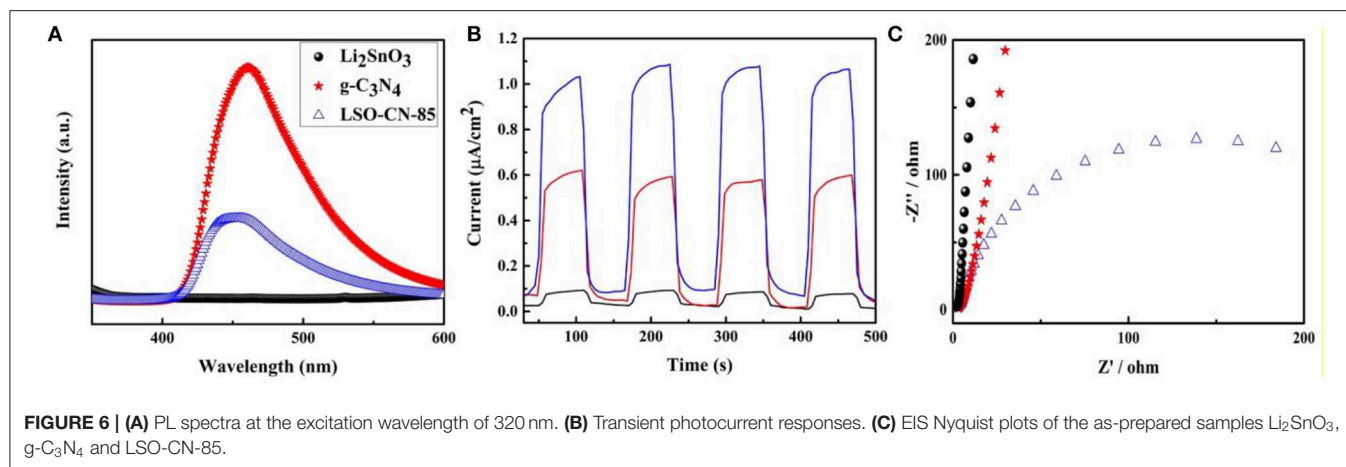

FIGURE 5 | (A) Photocatalytic degradation of RhB with as-synthesized samples under visible light ($\lambda \geq$ 420 nm); **(B)** The pseudo-first order kinetic fitting of the photodegradation of RhB; **(C)** The fitted kinetic constants for RhB photodegradation; **(D)** Cycling experiments of LSO-CN-85 for RhB photodegradation.

where C_0 and C are the RhB concentration in solution at time 0 and t, respectively. The quantity k is the fitted kinetic rate constant. It can be seen that the plots of the irradiation time t against $\ln\frac{C_0}{C}$ are nearly straight lines, which reveals that all the photocatalysts followed pseudo-first order kinetics in the photodegradation of the RhB solution. The kinetic rate

constants of Li$_2$SnO$_3$ and g-C$_3$N$_4$ were 0.0006 and 0.0057 min^{-1}, respectively. For the Li$_2$SnO$_3$/g-C$_3$N$_4$ heterojunctions, the corresponding kinetic rate constants of LSO-CN-70, LSO-CN-80, LSO-CN-85, LSO-CN-90, and LSO-CN-95 were fitted as 0.0208, 0.0203, 0.0302, 0.0167, and 0.0108 min^{-1}, respectively. The kinetic rate constant of the LSO-CN-85 was the highest,

FIGURE 6 | (A) PL spectra at the excitation wavelength of 320 nm. **(B)** Transient photocurrent responses. **(C)** EIS Nyquist plots of the as-prepared samples Li$_2$SnO$_3$, g-C$_3$N$_4$ and LSO-CN-85.

and was ∼50 and 5 times that of pure Li$_2$SnO$_3$ and g-C$_3$N$_4$. To evaluate the stability of the photocatalytic performance, cycling experiments of the heterojunction LSO-CN-85 were carried out. As indicated in **Figure 5D**, the photocatalytic activity exhibited no obvious loss after four successive cycles for the photodegradation of RhB solution, and the observed XRD patterns during the cycling photocatalytic experiments still matched well with pristine LSO-CN-85 (**Figure S2**), both suggesting that the LSO-CN heterojunction photocatalyst was stable during the photocatalytic reaction process.

To quantify the separation efficiency of the photo-induced carriers, measurements of solid photoluminescence, photocurrent responses and electrochemical impedance spectroscopy were performed. **Figure 6A** presents the PL spectra of Li$_2$SnO$_3$, g-C$_3$N$_4$ and LSO-CN-85 excited at 325 nm. For Li$_2$SnO$_3$, no obvious emission peak was observed in the range of 400–600 nm, whereas for g-C$_3$N$_4$, strong fluorescence intensity was centered at ∼460 nm. Generally, weaker emission intensity of a PL spectrum manifests higher separation efficiency of photo-induced carriers, implying a low recombination rate. For the heterojunction LSO-CN-85, the PL intensity was considerably lower than that of g-C$_3$N$_4$, indicating the strong suppression of the recombination of photo-induced carriers in the heterojunction.

Further, the photocurrent responses of the as-prepared samples were determined during four on/off visible light irradiation cycles in Na$_2$SO$_4$ electrolyte. As presented in **Figure 6B**, g-C$_3$N$_4$ had a markedly low transient photocurrent response because of the high recombination rate of photo-induced carriers, while Li$_2$SnO$_3$ exhibited the lowest photocurrent density, ascribed to its wide band gap. However, for the LSO-CN-85 heterostructure, the photocurrent density increased notably, indicating remarkably enhanced efficiency in the separation and transportation of photo-induced carriers. Next, EIS was performed to explore the conductive properties of the as-prepared samples under visible light (**Figure 6C**). As is well-known, in Nyquist plots, a smaller arc radius represents lower impedance and higher efficiency of charge transfer. Notably, the LSO-CN-85 heterostructure had a smaller arc radius than the parent compounds Li$_2$SnO$_3$ and g-C$_3$N$_4$, which

further testified to the effective separation of photo-induced carriers after forming the heterojunction. Hence, based on the above results, the Li$_2$SnO$_3$/g-C$_3$N$_4$ heterostructure was able to promote the transfer and separation of the photo-induced carriers, leading to the enhancement of photocatalytic activity under visible light.
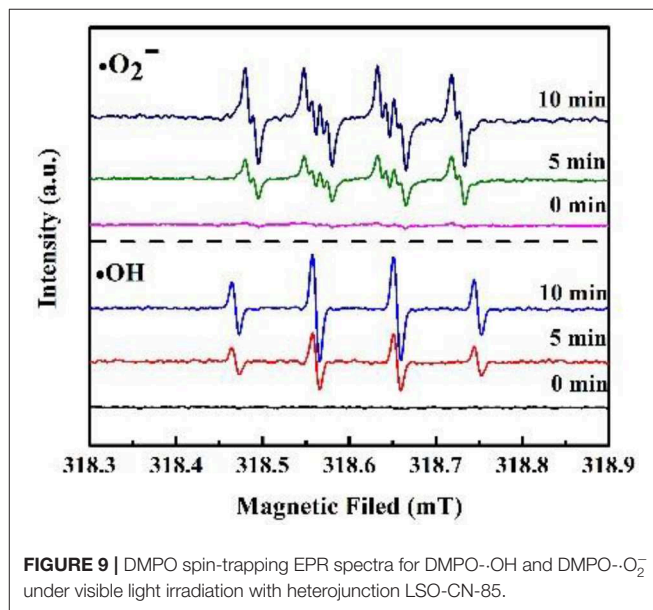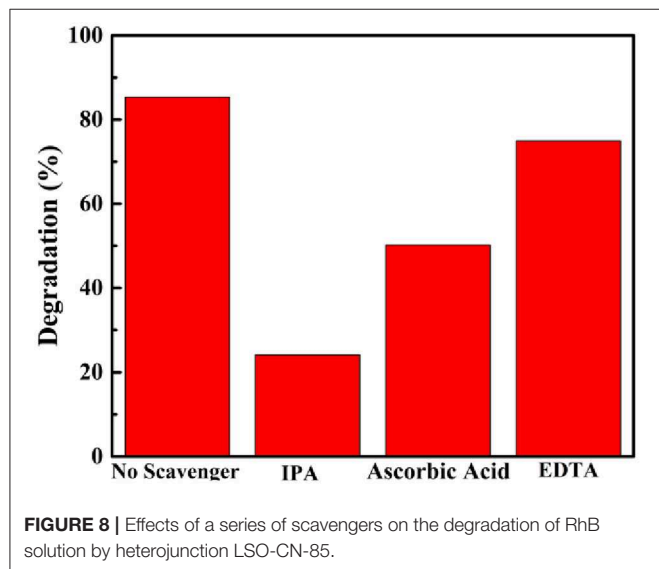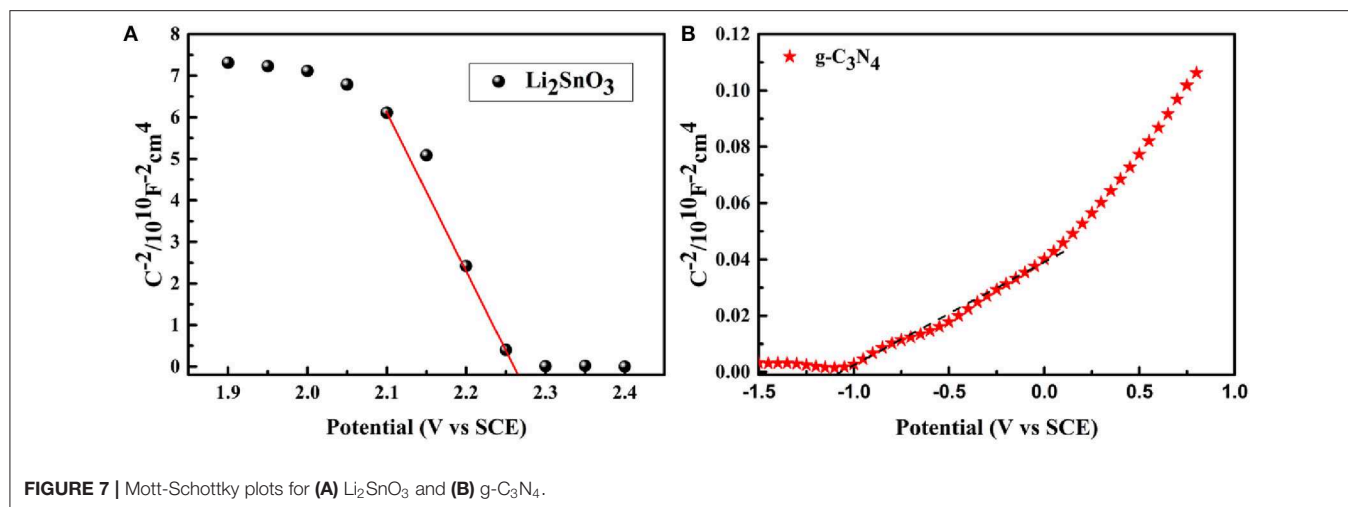
Mott-Schottky measurement was performed to evaluate the oxidation capability of the as-synthesized catalysts. The flat-band potentials were calculated by the Mott-Schottky equation (Gelderman et al., 2007; Cho et al., 2009; Boltersdorf et al., 2016):

$$\frac{1}{C^2} = \left(\frac{2}{\varepsilon_r \varepsilon_0 N_d e}\right) \times \left(V - V_{fb} - \frac{\kappa_B T}{e}\right)$$

where C is the space charge capacitance, ε_r and ε_0 are the dielectric constant of the semiconductor and the permittivity in a vacuum, e is the electronic charge, N_d is the carrier density, and V, V_{fb}, κ_B and T are the applied voltage, flat-band potential, Boltzmann constant and temperature, respectively. Here, V_{fb} was obtained as the x-intercept of the Mott-Schottky plots ($\frac{1}{C^2} = 0$) as a function of the applied potential. Meanwhile, the flat-band potential V_{fb} corresponds to the conduction band potential for an n-type semiconductor and the valence band edge potential for a p-type semiconductor. As indicated from the positive and negative slopes of the Mott-Schottky plots in **Figures 7A,B**, Li$_2$SnO$_3$ was a p-type semiconductor, while g-C$_3$N$_4$ was of the n-type. The corresponding V_{fb} of Li$_2$SnO$_3$ and g-C$_3$N$_4$ were determined to be 2.27 and −1.1 V vs. saturated calomel electrode (SCE), respectively, and these potentials relative to SCE were calibrated to the reversible hydrogen electrode (RHE) potentials through the following equation (Ke et al., 2017; Lin et al., 2018; Xu et al., 2019):

$$V_{RHE} = V_{SCE} + 0.059\, pH + V_{SCE}^0$$

where V_{RHE} is the calibrated potential vs. RHE, V_{SCE}^0 equals 0.245 V, and V_{SCE} are the obtained experimental values. Thus, the V_{fb} of Li$_2$SnO$_3$ and g-C$_3$N$_4$ were 2.92 and −0.45 V vs. RHE after calibration. Herein, the flat-band potential (defined as the quasi-Fermi level) is adopted to be 0.1 V below the conduction band

FIGURE 7 | Mott-Schottky plots for **(A)** Li$_2$SnO$_3$ and **(B)** g-C$_3$N$_4$.

FIGURE 8 | Effects of a series of scavengers on the degradation of RhB solution by heterojunction LSO-CN-85.

FIGURE 9 | DMPO spin-trapping EPR spectra for DMPO-·OH and DMPO-·O$_2^-$ under visible light irradiation with heterojunction LSO-CN-85.

minimum (CBM) or above the valence band maximum (VBM) for n-type and *p*-type semiconductors, respectively. Therefore, the final VBM of Li$_2$SnO$_3$ and CBM of g-C$_3$N$_4$ were 3.02 and −0.55 V, respectively. Referring to the estimated optical band gaps from the UV-vis DRS curves, the CBM of Li$_2$SnO$_3$ and VBM of g-C$_3$N$_4$ were calculated to be −0.62 and 2.20 V, respectively.

Trapping experiments of reactive species during the photocatalytic process were carried out to explore the mechanism of the LSO-CN-85 heterojunction. As shown in **Figure 8**, a dramatic suppression of photodegradation efficiency was observed after adding IPA and ascorbic acid, manifesting that and were the main participants in the photocatalytic reaction. In contrast, the introduction of EDTA had only a weak influence on the photodegradation rates, demonstrating that h^+ played a minor role in degrading the RhB solution. The reactive species were also detected using fluorescence spectroscopy. The increase of fluorescence intensity with prolonged irradiation

time was consistent with the results of the trapping experiments (**Figure S3**). To further investigate the active species ·OH and ·O$_2^-$ during the photocatalytic process, EPR measurements were performed. As presented in **Figure 9**, it could be seen that no EPR signal was detected in the darkness. However, the signal of ·OH and ·O$_2^-$ were increased remarkably, when the light was on. These results further confirmed the existence of ·OH and ·O$_2^-$ during the photocatalytic process.

Based on the above analysis, the proposed photocatalytic mechanism of the LSO-CN-85 heterojunction is presented in **Figure 10**. As revealed by the results of the Mott-Schottky measurements and UV-vis DRS experiments, the band alignments of *p*-type Li$_2$SnO$_3$ and g-C$_3$N$_4$ before formation of an interface were as presented in **Figure 10a**. First, when the *p*-type Li$_2$SnO$_3$ and g-C$_3$N$_4$ were combined to form the *p-n* heterostructure, the Fermi levels of Li$_2$SnO$_3$ tended to rise up
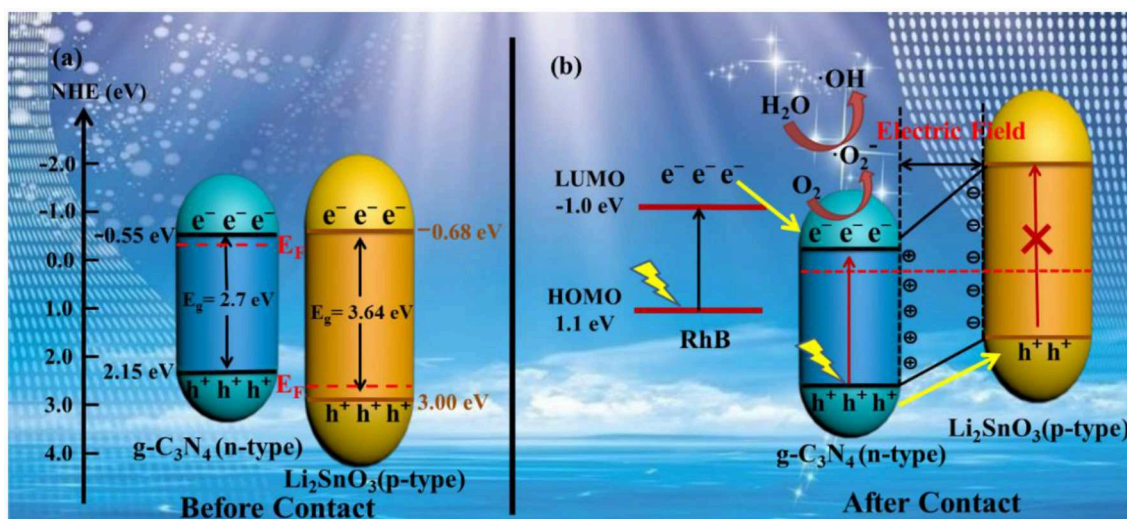
FIGURE 10 | Schematic of charge transfer between *p*-type Li$_2$SnO$_3$ and *n*-type g-C$_3$N$_4$ **(a)** before contact and **(b)** after contact forming the *p-n* heterojunction.

and the Fermi levels of g-C$_3$N$_4$ tended to descend to reach an equilibrium state. As a result, the CB edge of Li$_2$SnO$_3$ was higher than that of g-C$_3$N$_4$ and a built-in electric field was generated in the space charge region containing negatively charged Li$_2$SnO$_3$ and positively charged g-C$_3$N$_4$ (**Figure 10b**). Second, once the Li$_2$SnO$_3$/g-C$_3$N$_4$ heterojunction was irradiated with visible light, photo-induced electrons and holes were generated in the g-C$_3$N$_4$. However, the photogenerated electrons and holes could not be excited in the Li$_2$SnO$_3$ owing to its intrinsic wide band gap. As a results, the inner electric field at the *p-n* heterojunction interface will push the holes in the VB of g-C$_3$N$_4$ toward the VB of Li$_2$SnO$_3$. Meanwhile, the generated electrons remained in the conduction band of g-C$_3$N$_4$, where the accumulated electrons reacted with O$_2$ adsorbed on the surface of the heterojunction to form and, which in turn degraded RhB in the aqueous solution. Therefore, in such a way, the photogenerated electrons and holes were efficiently separated and the recombination rate was decreased. In addition, the dye sensitization effect was also considered in this system. The photoexcited electrons on the LOMO level of RhB molecule (Dong et al., 2014) were prone to transfer to the CB of g-C$_3$N$_4$, resulting in the increased aggregation of electrons and further enhanced the performance of the photodegradation.

CONCLUSION

A novel LSO-CN heterojunction photocatalyst, comprising *p*-type Li$_2$SnO$_3$ and n-type g-C$_3$N$_4$, was successfully prepared by a facile calcining method. The obtained heterojunctions LSO-CN were characterized by PXRD, SEM, TEM, FT-IR, and UV-vis DRS. The optimum photodegradation rate was that of the heterojunction LSO-CN-85, i.e., 86% degradation of RhB after 60 min of visible light irradiation, which was ~5 times that of g-C$_3$N$_4$. The photo-induced and active

radicals played the dominant role in the photocatalytic RhB degradation over the LSO-CN-85 heterojunction photocatalyst. Photoelectrochemical performance measurements were carried out to elucidate the photocatalytic mechanism. The enhanced photocatalytic performance could be attributed to the successful preparation of a *p-n* heterojunction between Li$_2$SnO$_3$ and g-C$_3$N$_4$, which greatly promoted the efficient separation of photo-induced carriers.

DATA AVAILABILITY STATEMENT

All datasets generated for this study are included in the article/**Supplementary Material**.

AUTHOR CONTRIBUTIONS

Specifically, YL and DY proposed this topic and design of the project. BZ and MW completed the characterization part. MW, QY, and XL completed the experimental part. YW analyzed the results. DY, BZ, and YL composed the manuscript. All authors participated in the discussions of the results and made important contributions on this work.

FUNDING

SUPPLEMENTARY MATERIAL

REFERENCES

Boltersdorf, J., Zoellner, B., Fancher, C. M., Jones, J. L., and Maggard, P. A. (2016). Single and double site substitutions in mixed metal oxides: adjusting the band edges toward the water redox couples. *J. Phys. Chem. C.* 120, 19175–19188. doi: 10.1021/acs.jpcc.6b05758

Chen, C. C., Ma, W. H., and Zhao, J. C. (2010). Semiconductor-mediated photo-degradation of pollutants under visible light irradiation. *Chem. Soc. Rev.* 39, 4206–4219. doi: 10.1039/b921692h

Cho, I. S., Kwak, C. H., Kim, D. W., Lee, S. W., and Hong, K. S. (2009). Photophysical, photoelectrochemical and photocatalytic properties of novel SnWO4 oxide semiconductors with narrow band gaps. *J. Phys. Chem. C.* 113, 10647–10653. doi: 10.1021/jp901557z

Damasiewicz, M. J., Polkinghorne, K. R., and Kerr, P. G. (2012). Water quality in conventional and home haemodialysis. *Nat. Rev. Nephrol.* 8, 725–734. doi: 10.1038/nrneph.2012.241

Dong, H. J., Chen, G., Sun, J. X., Feng, Y. J., Li, C. M., Xiong, G. H., et al. (2014). Highly effective photocatalytic properties and interfacial transfer efficiencies of charge carriers for the novel Ag2CO3/AgX heterojunctions achieved by surface modification. *Dalton Trans.* 43, 7282–7289. doi: 10.1039/C4DT00058G

Dong, Z. J., Pan, J. Q., Jiang, Z. Y., Zhao, C., Wang, J. J., Song, C. S., et al. (2018). The *p-n* type Bi5O7I-modified porous C3N4 nano-heterojunction for enhanced visible light photocatalysis. *J. Alloy. Compd.* 747, 788–795. doi: 10.1016/j.jallcom.2018.03.112

Dursun, S., Kaya, I. C., Kalem, V., and Akyildiz, H. (2018). UV/visible Light Active CuCrO2 nanoparticle-SnO2 nanofiber *p-n* heterostructured photocatalysts for photocatalytic applications. *Dalton Trans.* 47, 14662–14678. doi: 10.1039/C8DT02850H

Gelderman, K., Lee, L., and Donne, S. W. (2007). Flat band potential of a semiconductor using the mott schottky equation. *J. Chem. Edu.* 84, 685–688. doi: 10.1021/ed084p685

Guo, F., Shi, W. L., Wang, H. B., Huang, H., Liu, Y., and Kang, Z. H. (2017). Fabrication of a CuBi2O4/g-C3N4 *p-n* heterojunction with enhanced visible light photocatalytic efficiency toward tetracycline degradation. *Inorg. Chem. Front.* 4, 1714–1720. doi: 10.1039/C7QI00402H

Guo, Y., Li, J. H., Gao, Z. Q., Zhu, X., Liu, Y., Wei, Z. B., et al. (2016). A simple and effective method for fabricating novel *p-n* heterojunction photocatalyst g-C3N4/Bi4Ti3O12 and its photocatalytic performances. *Appl. Catal. B: Environ.* 192, 57–71. doi: 10.1016/j.apcatb.2016.03.054

Hafeez, H. Y., Lakhera, S. K., Narayanan, N., Harish, S., Hayakawa, Y., Lee, B. K., et al. (2019). Environmentally sustainable synthesis of a CoFe2O4-TiO2/rGO ternary photocatalyst: a highly efficient and stable photocatalyst for high production of hydrogen (Solar Fuel). *ACS Omega.* 4, 880–891. doi: 10.1021/acsomega.8b03221

Hailili, R., Wang, Z. Q., Li, Y. X., Wang, Y. H., Sharma, V. K., Gong, X. Q., et al. (2018). Oxygen vacancies induced visible light photocatalytic activities of CaCu3Ti4O12 with controllable morphologies for antibiotic degradation. *Appl. Catal. B Environ.* 221, 422–432. doi: 10.1016/j.apcatb.2017.09.026

Haque, F., Daeneke, T., Zadeh, K. K., and Ou, J. Z. (2018). Two-dimensional transitional metal oxide and chalcogenide based photocatalysts. *Nano-Micro Lett.* 10, 23–49. doi: 10.1007/s40820-017-0176-y

Hou, Y., Wen, Z. H., Cui, S. M., Guo, X. R., and Chen, J. H. (2013). Constructing 2D porous graphitic C3N4 nanosheets/nitrogen doped graphene/layered MoS2 ternary nanojunction with enhanced photoelectrochemical activity. *Adv. Mater.* 25, 6291–6279. doi: 10.1002/adma.201303116

Howard, J., and Holzwarth, N. A. W. (2016). First principles simulations of the porous layered calcogenides Li2+xSnO3 and Li2+xSnS3. *Phys. Rev. B.* 94, 064108–064120. doi: 10.1103/PhysRevB.94.064108

Ke, J., Liu, J., Sun, H. Q., Zhang, H. Y., Duan, X. G., Liang, P., et al. (2017). Facile assembly of Bi2O3/Bi2S3/MoS2 n-p heterojunction with layered n-Bi2O3 and p-MoS2 for enhanced photocatalytic water oxidation and pollutant degradation. *Appl. Catal. B: Environ.* 200, 47–55. doi: 10.1016/j.apcatb.2016.06.071

Lei, F. C., Sun, Y. F., Liu, K. T., Gao, S., Liang, L., Pan, B. C., et al. (2014). Oxygen vacancies confined in ultrathin indium oxide porous sheets for promoted visible light water splitting. *J. Am. Chem. Soc.* 136, 6826–2829. doi: 10.1021/ja501866r

Li, X. B., Xiong, J., Gao, X. M., Huang, J. T., Feng, Z. J., Chen, Z., et al. (2019). Recent advances in 3D g-C3N4 composite photocatalysts for photocatalytic water splitting, degradation of pollutants and CO2 reduction. *J. Alloy. Compd.* 802, 196–209. doi: 10.1016/j.jallcom.2019.06.185

Li, Y. X., Hou, Y. L., Fu, Q. Y., Peng, S. Q., and Hu, Y. H. (2017). Oriented growth of ZnIn2S4/In(OH)3 heterojunction by a facile hydrothermal transformation for efficient photocatalytic H2 production. *Appl. Catal. B Environ.* 206, 726–733. doi: 10.1016/j.apcatb.2017.01.062

Li, Y. Y., Wu, M. J., Li, Q. Q., Zeng, H. L., Zhang, T., Shen, J. F., et al. (2019). Novel high efficiency layered oxide photocatalyst Li2SnO3 for rhodamine B and tetracycline degradation. *Catalysts.* 9, 712–724. doi: 10.3390/catal9090712

Liang, Q., Jin, J., Liu, C. H., Xu, S., and Li, Z. Y. (2017). Constructing a novel *p-n* heterojunction photocatalyst LaFeO3/g-C3N4 with enhanced visible light driven photocatalytic activity. *J. Alloy. Compd.* 709, 542–548. doi: 10.1016/j.jallcom.2017.03.190

Lin, R., Wan, J. W., Xiong, Y., Wu, K. L., Cheong, W. C., Zhou, G., et al. (2018). Quantitative study of charge carrier dynamics in well-defined WO3 nanowires and nanosheets: insight into the crystal facet effect in photocatalysis. *J. Am. Chem. Soc.* 140, 9078–9082. doi: 10.1021/jacs.8b05293

Liu, H. J., Du, C. W., Li, M., Zhang, S. S., Bai, H. K., Yang, L., et al. (2018). One-pot hydrothermal synthesis of SnO2/BiOBr heterojunction photocatalysts for the efficient degradation of organic pollutants under visible light. *ACS Appl. Mater. Interfaces.* 10, 28686–28694. doi: 10.1021/acsami.8b09617

Lu, L. Y., Wang, G. H., Zou, M., Wang, J., and Li, J. (2018). Effects of calcining temperature on formation of hierarchical TiO2/g-C3N4 hybrids as an effective Z-scheme heterojunction photocatalyst. *Appl. Surf. Sci.* 441, 1012–1023. doi: 10.1016/j.apsusc.2018.02.080

Nguyen, T. B., Huang, C. P., and Doong, R. (2019). Photocatalytic degradation of bisphenol A over a ZnFe2O4/TiO2 nanocomposite under visible light. *Sci. Total Environ.* 646, 745–756. doi: 10.1016/j.scitotenv.2018.07.352

Ong, W. J., Tan, L. L., Ng, Y. H., Yong, S. T., and Chai, S. P. (2016). Graphitic carbon nitride (g-C3N4)-based photo-catalysts for artificial photo-synthesis and environmental remediation: are we a step closer to achieving sustainability? *Chem. Rev.* 116, 12, 7159–7329. doi: 10.1021/acs.chemrev.6b00075

Osada, M., and Sasaki, T. (2009). Exfoliated oxide nanosheets: new solution to nanoelectronics. *J. Mater. Chem.* 19, 2503–2511. doi: 10.1039/b820160a

Pan, C. S., Xu, J., Wang, Y. J., Li, D., and Zhu, Y. F. (2012). Dramatic activity of C3N4/BiPO4 photocatalyst with core/shell structure formed by self-assembly. *Adv. Funct. Mater.* 22, 1518–1524. doi: 10.1002/adfm.201102306

Qiao, X. Q., Zhang, Z. W., Hou, D. F., Li, D. S., Liu, Y. L., Lan, Y. Q., et al. (2018). Tunable MoS2/SnO2 *p-n* heterojunctions for an efficient trimethylamine gas sensor and 4-nitrophenol reduction catalyst. *ACS Appl. Mater. Interfaces* 6, 12375–12384. doi: 10.1021/acssuschemeng.8b02842

Shannon, M. A., Bohn, P. W., Elimelech, M., Georgiadis, J. G., Marinas, B. J., and Mayers, A. M. (2008). Sceicne and technology for water purification in the coming decades. *Nature.* 452, 301–310. doi: 10.1038/nature06599

Wang, H., Sun, Y. J., He, W. J., Zhou, Y., Lee, S. C., and Dong, F. (2018a). Visible light induced electron transfer from a semiconductor to an insulator enables efficient photocatalytic activity on insulator-based heterojunctions. *Nanoscale* 10, 15513–15520. doi: 10.1039/C8NR03845G

Wang, H., Sun, Y. J., Jiang, G. M., Zhang, Y. X., Huang, H. W., Wu, Z. B., et al. (2018b). Unraveling the mechanisms of visible light photocatalytic NO purification on earth abundant insulator based core shell heterojunctions. *Environ. Sci. Technol.* 52, 1479–1487. doi: 10.1021/acs.est.7b05457

Wang, H., Zhang, X. D., and Xie, Y. (2019). Photoresponsive polymeric carbon nitride based materials: design and application. *Mater. Today.* 23, 72–86. doi: 10.1016/j.mattod.2018.05.001

Wang, J., Zhang, G. K., Li, J., and Wang, K. (2018). Novel three dimensional flowerlike BiOBr/Bi2SiO5 *p-n* heterostructured nanocomoposite for degradation of tetracycline: enhanced visible light photocatalytic activity and mechanism. *ACS Sust. Chem. Eng.* 6, 14221–14229. doi: 10.1021/acssuschemeng.8b02869

Wang, Q. F., Huang, Y., Miao, J., Zhao, Y., and Wang, Y. (2012). Synthesis and properties of Li2SnO3/polyaniline nanocomposites as negative electrode material for lithium-ion batteries. *Appl. Surface Sci.* 258, 9896–9901. doi: 10.1016/j.apsusc.2012.06.047

Wang, X. C., Maeda, K., Thomas, A., Takanabe, K., Xin, G., Carlsson, J. M., et al. (2009). A metal free polymeric photocatalyst for hydrogen production from water under visible light. *Nat. Mater.* 8, 76–80. doi: 10.1038/nmat2317

Wen, J. Q., Xie, J., Chen, X. B., and Li, X. (2017). A review on g-C3N4 based photo-catalysts. *Appl. Surface Sci.* 391, 72–123. doi: 10.1016/j.apsusc.2016.07.030

Wen, X. J., Niu, C. G., Zhang, L., and Zeng, G. M. (2017). Novel *p-n* heterojunction BiOI/CeO2 photocatalyst for wider spectrum visible light photocatalytic degradation of refractory pollutants. *Dalton Trans.* 40, 4982–4993. doi: 10.1039/C7DT00106A

Wu, Z. H., Liu, J., Tian, Q. Y., and Wu, W. (2017). Efficient visible light formaldehyde oxidation with 2D *p-n* heterostructure of BiOBr/BiPO4 nanosheets at room temperature. *ACS Sust. Chem. Eng.* 5, 5008–5017. doi: 10.1021/acssuschemeng.7b00412

Xie, Z. J., Feng, Y. P., Wang, F. L., Chen, D. N., Zhang, Q. X., Zeng, Y. Q., et al. (2018). Construction of carbon dots modified MoO3/g-C3N4 Z-scheme photocatalyst with enhanced visible light photocatalytic activity for the degradation of tetracycline. *Appl. Catal. B: Environ.* 229, 96–104. doi: 10.1016/j.apcatb.2018.02.011

Xu, Z. Q., Guan, Z. G., Yang, J. J., and Li, Q. Y. (2019). Band positions and photoelectrochemical properties of solution processed silver substituted Cu2ZnSnS4 photocathode. *ACS Appl. Energy Mater.* 2, 2779–2785. doi: 10.1021/acsaem.9b00116

Yin, X. L., Li, L. L., Li, D. C., Wei, D. H., Hu, C. C., and Dou, J. M. (2019). Room temperature synthesis of CdS/SrTiO3 nanodots-on-nanocubes for efficient photocatalytic H2 evolution from water. *J. Coll. Interf. Sci.* 536, 694–700. doi: 10.1016/j.jcis.2018.10.097

Zeng, Y., Guo, N., Li, H. Y., Wang, Q. Y., Xu, X. Q., Yu, Y., et al. (2019). A novel route to manufacture WO3@MoS2 *p-n* heterostructure hollow tubes with enhanced photocatalytic activity. *Chem. Commun.* 55, 683–686. doi: 10.1039/C8CC08614A

Zhang, L. P., Wang, G. H., Xiong, Z. Z., Tang, H., and Jiang, C. J. (2018). Fabrication of flower like direct Z-scheme beta-Bi2O3/g-C3N4 photocatalyst with enhanced visible light photoactivity for rhodamine B degradation. *Appl. Surf. Sci.* 436, 162–171. doi: 10.1016/j.apsusc.2017.11.280